

HELICOPTER BLADE TWIST CONTROL THROUGH SMA TECHNOLOGY: OPTIMAL SHAPE PREDICTION, TWIST ACTUATOR REALISATION AND MAIN ROTOR ENHANCED PERFORMANCE COMPUTATION

Antonio Pagano, Salvatore Ameduri, C.I.R.A. ScpA, Capua (CE), Italy
V. Cokonaj, AERnova AEROSPACE, Bilbao, Spain
A. Prachař, VZLU, Praha, Czech Republic
Z. Zachariadis, D. Drikakis, CRANFIELD University, Cranfield, United Kingdom

Abstract

The improvement of helicopter performance represents a challenging target because of the several involved disciplinary areas involved: aerodynamics, aeroacoustics, aeroelasticity, stability/manoeuvrability, propulsion. Among the many and different systems constituting a helicopter, a remarkable influence on the overall efficiency may be attributed to the main rotor; thus, more and more efforts are spent to improve its features, both in hover and forward flight. The classical design strategy aimed at enhancing the rotor efficiency is based on the passive optimization of the rotor blade geometry (i.e. airfoil shape, span length, chord and twist distribution, planform, tip shape). However, due to the different regimes the rotor has to work in, it is not possible to identify a unique configuration, optimal for any flight condition. This leads to consider solutions, belonging to "adaptive" typology, able to affect rotor performance at several regimes: conventional and innovative actuators, locally integrated within the blade to change its shape, dampers for vibration control, local suction to modify the aerodynamic field, are just some examples of the strategies that are under investigation. According to this trend, within the FRIENDCOPTER European Integrated Project^[1], the goal of enhancing the Figure of merit of the BO-105 rotor^[2] has been accomplished by affecting the blade twist and the airfoil camber through SMA based actuators. Firstly, numerical investigations have been performed to identify the blade geometry (airfoils and blade tip shape) able to guarantee an optimal Figure of merit in the hover condition; secondly, the design of a SMA based on an actuator able to produce the required twist has been carried out by adopting a dedicated FE approach (MSC/Marc software with the SMA Brinson model implemented); then, a laboratory specimen of the actuator has been manufactured and tested in order to validate numerical predictions; and, finally, the effective benefits in terms of Figure of merit has been estimated.

1. INTRODUCTION

"Adaptive Material and Structure" concepts, due to envisaged benefits in terms of active modification / adaptation of critical design parameters, are more and more investigated and play a fundamental role for engineering applications in the rotorcraft field.^{[3],[4]}

Due to the large transmittable forces and deformations, Shape Memory Alloys (SMA) belonging to the mentioned Adaptive Material family, have found a wide range of applications, from aerospace to civil field, from surgery to the electronics, and so on... In practice, the phase transformation characterising these alloys, depending both on temperature and stress field, can be exploited to recover strain (Shape Memory Effect; use as actuator element) or to endure to large deformations (Super Elastic Effect; use as non linear elastic spring).^{[5]-[8]}

Several numerical and experimental studies have

addressed blade twist designs because of envisaged benefits both in terms of flight envelope extension and noise and vibration attenuation. Among these studies many are based on the concept based on a SMA torsional rod. Its theoretical modelling and experimental testing has been investigated in [9]-[10] and an application for deflecting a tab for in-flight tracking of helicopter rotor blades has been presented in [11]. The torsional SMA technology has been also proposed in [12]-[13] for the tiltrotor where the blade twist requirements are different for hover and cruise flight.

Within the FRIENDCOPTER Integrated Project (2004-2009), a research initiative conceived in the context of the VI Framework Programme of the European Community, the requirement of mitigating the environmental impact of helicopters has been addressed globally in the sense that several aspects (such as noise abatement, vibration reduction, fuel consumption) have been studied in parallel with different approaches among which there is the active blade control. In this work, two topics are presented and discussed: the aerodynamic optimization of a

blade section which is able to modify its camber by means of an actuator and the design of a SMA based static twist concept, aimed at extending the helicopter flight envelope. The latter device is based on a SMA rod which is integrated in the spanwise direction within the blade structure at different positions. The actuator, when heated, transmits a torque couple which induces twist onto the blade. The twist variation due to the SMA device activation has been predicted by a FE approach (MSC/Marc software implemented with the SMA Brinson model).

Finally, rotor performance in hover has been estimated with the actuator in power on and off positions, highlighting benefits coming from several spanwise integrations/distributions of the SMA device.

2. THE ROTOR GEOMETRIES

In the FRIENDCOPTER project three rotor geometries are considered: the full scale rotor, its 1:2.5 model scale rotor and a new model scale rotor with parabolic tip.^[14] The full scale rotor and the original model scale rotor are equipped with the NACA23012 airfoil and have a rectangular planform. The new model scale rotor (see Figure 1) mounts the ONERA OA209 airfoil on the outer part of the blade and the tip parabolic shape comes from the tip geometry of the ONERA/EC 7AD rotor.^[15]

While the original model scale rotor serves as reference for the actuators design (both for airfoil camber and static twist modifications), the new model scale rotor includes passive optimization features and eventually it will accommodate the installation of the actuators assessed in section 3 and 4.

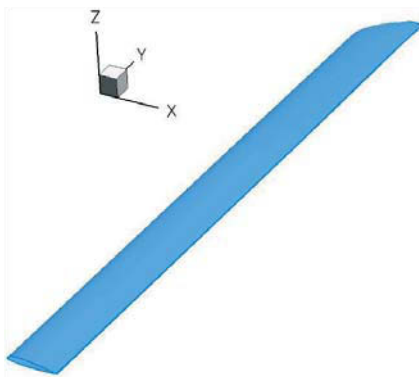


Figure 1. View of the new model scale rotor blade with parabolic tip.

3. THE OPTIMAL CAMBER OF THE BLADE INNER SECTION

As it can be seen later, the replacement of the

NACA23012 airfoil with the ONERA OA209 airfoil in the outer part of the blade significantly improves the rotor performances. The need for a better airfoil in the inboard part of the blade is approached by considering as reference airfoil the well known ONERA OA312 to be subsequently modified by an actuator able to alter its camber. This task is articulated in two steps: the reference airfoil is aerodynamically characterized for given conditions and the camber line is optimized according to given objectives and constraints.

The optimization is performed by a numerical process where several software components are involved. The mesh generation is accomplished by a commercial software package (Pointwise Gridgen).^[16] Since the optimization is expected to require the evaluation of a large amount of different airfoils derived from the reference geometry, the computational grids are not re-generated but an *ad-hoc* code which smoothly deforms the reference grid is embedded into the numerical process. This fast and robust analytic mesh deformation method is based on an arc length transfinite interpolation and propagates geometric perturbations into an existing high quality initial grid while preserving the initial grid characteristics. A C-shaped structured quadrilateral computational grid fulfilling usual requirements for turbulent calculations (refinement in the near wall region, etc.) is generated around the ONERA OA312 airfoil.

As far as the choice of the CFD solver is concerned, the need of having access to the source code for any code adaptation to the optimization process has led to choose an in-house partner code rather than a commercial code.

The fundamental feature of the CFD solver is a modified HLLC (Harten, Lax and van Leer for Contact waves) Riemann solver^[17] that has been incorporated into the CFD code CNS3D^{[18],[19]} to properly account for the turbulence transport quantities. WENO 5th-order schemes^[20] have been used in the inviscid flux reconstruction discretization, while the viscous terms are discretized using second-order central schemes. The turbulence transport quantities are modelled via the implementation of the $k-\omega$ model. Time integration is performed by a Newton method that solves the unfactored implicit equations. The implicit operator is constructed through the implementation of the flux vector splitting method of Steger-Warming^[21] along with contributions resulting from the thin layer viscous Jacobians and the turbulence source terms. Convergence to steady state is accelerated with a point Gauss-Seidel relaxation technique.^[22]

The reference airfoil performance is predicted for a range of Mach numbers and angles of attack typical of blade inboard sections by applying the Menter

SST k- ω turbulence model at a Reynolds number satisfying the relation $Re/Mach \approx 8 \times 10^6$ and with a free stream turbulence intensity of 0.5%. As an example of the ONERA OA312 airfoil characterization, Figures 2-3 show the coefficients of lift, drag and pitching moment.

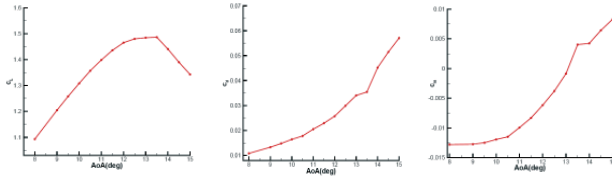


Figure 2. Coefficients of lift (left), drag (middle) and pitching moment (right). Mach = 0.4.

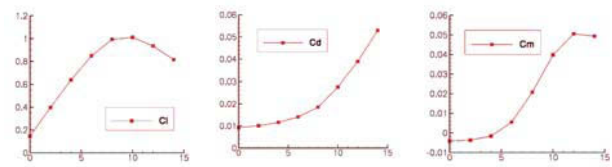


Figure 3. Coefficients of lift (left), drag (middle) and pitching moment (right). Mach = 0.5.

As a verification example, Table 1 compares for Mach=0.4 the computed results at 9.8 and 10.5 degrees of AoA against experiments. It is noteworthy that the computed aerodynamic loads are in a close agreement with the experimental values.

	AoA (deg.)	C_l	C_m	C_d
Experiment	9.8	1.27	-0.0122	0.0137
	10.5	1.34	-0.0113	0.0149
Computation	9.8	1.29	-0.0125	0.0158
	10.5	1.35	-0.0115	0.0177

Table 1. Comparison between experimental and computational C_l , C_m and C_d .

The optimization task is performed by using a Tabu Search (TS) algorithm that has been developed by Jaeggi *et al.*^[23] A simple and efficient geometry parameterization technique is incorporated into the numerical process. The parameterization of the initial geometry is the transformation of the active part of the airfoil into the parameterized design vector. For the employed actuator design the active chord, x_a , may be varied in the range of 80% to 20%. Furthermore, it is assumed that upward and downward actuation results in the same deflection shape neglecting asymmetries from aerodynamic loading or actuator design. Furthermore, the chord length of the airfoil is assumed to remain constant. With the above assumptions, a sixth order polynomial is employed to parameterize the

deformed camber line:

$$(1) \quad f(\bar{x}) = a_6 \bar{x}^6 + a_5 \bar{x}^5 + a_4 \bar{x}^4 + a_3 \bar{x}^3 + a_2 \bar{x}^2 + a_1 \bar{x} + a_0$$

where $\bar{x} = \frac{x - (1 - x_a)}{c - (1 - x_a)}$ and c being the chord of the airfoil.

The authority of the actuator is introduced by the maximum achievable non-dimensional deflection $z_{\max}^* = z_{\max} / c$ that varies depending on the actuator design; $-0.01 \leq z_{\max}^* \leq 0.01$. The polynomial function, Eq. (1), is scaled with the actuator authority thus forming the actual shape function that is superimposed to the skeleton line of the underlying airfoil:

$$(2) \quad \Phi(\bar{x}) = z_{\max}^* f(\bar{x}) .$$

The produced design vector consists of 8 variables in total, of which the first two describe the chordwise length of the active part of the airfoil and the authority of the piezoelectric actuator, whereas the next 6 variables, the coefficients of the polynomial function, define the actual shape of the camber.

All of the software components previously described are part of the computational system called MOBID (Multi-OBjective Integrated Design) assessed at Cranfield University.

The optimization effort is undertaken in order to identify the aerodynamic effectiveness in terms of servo effect C_m or direct lift effect C_l of the actuation concept when applied to the ONERA OA312 airfoil. In general the desired characteristics for an airfoil to be used in the inboard region of a main rotor blade are (1) the highest possible maximum lift coefficients at Mach numbers from 0.3 to 0.5 for increased blade loading on the retreating side of the rotor disk, (2) pitching moment coefficients nearly equal to zero, for low blade torsion loads.

From the computed polars presented in Figure 2, it can be seen that the maximum lift, $C_l = 1.486$, occurs at 13.5 degrees for which $C_m = 0.004$ and $C_d = 0.0354$. Therefore the design goals of the present investigation are set to be: $C_l > 1.5$ and $C_m \approx 0$.

Having identified the design goals, the optimization task can now be described as a constrained bi-objective minimization problem, with the following objective functions:

$$(3) \quad f_1 = -c_l$$

$$(4) \quad f_2 = |c_m|$$

Obvious constraints of the current optimization task are the active part of the airfoil and the authority of the actuator;

$$(5) \quad 20\% \leq x_a \leq 80\%$$

$$(6) \quad -0.01 \leq z_{\max}^* \leq 0.01$$

A not so obvious constraint is related to the amplitude of the polynomial itself. It is imperative that the maximum deflection of the polynomial shape does not exceed unity, in order to prevent large deformations that are not realizable by the actuator. This constraint is clearly satisfied by setting $a_0 = 0$ and most importantly by;

$$(7) \quad \sum |a_n| \leq 1, \text{ with } n = 1, \dots, 6$$

Besides the identification and definition of the objectives and constraints of the optimization problem, the number of CFD iterations in conjunction with the number of the grid nodes has great impact on the computational cost as the optimization process progresses. In order to keep the optimization cost to a minimum without compromising in accuracy, computation grids including 280×90 control volumes are employed.

The findings of the optimization process are summarized in Figure 4 where the Pareto front displays numerous discontinuities because of the non-linear nature of the aerodynamic problem. The observed gaps in the search pattern are attributed to geometrically and aerodynamically unfeasible designs as well as airfoil designs of poor aerodynamic performance. It is clear that the design space is strongly constrained in the region where designs with the lowest absolute pitching moment occur. In fact, the resulted feasible designs have similar values of this objective function and the trade-off surface in this area is almost horizontal, indicating that small improvements in pitching moment are obtained at the cost of lift deterioration. Furthermore, the achievable trade-off between lift and minimum absolute pitching moment is manifested through a clear discontinuity in the Pareto front.

In Figure 4 six designs are outlined and their geometrical characteristics are individually displayed in Figures 5-10. These designs correspond to airfoils with, respectively, the highest lift coefficient, the lowest, in magnitude, pitching moment coefficient and some optimal compromises. The geometry is quite different to the baseline geometry and in addition there are significant differences amongst them. The airfoil design for the highest lift has a completely different camber variation, compared to

the design for lowest absolute pitching moment. In contrast, the compromise designs display similar geometrical characteristics with each other. There are some general geometrical characteristics that distinguish the optimum designs from the baseline airfoil design. Geometries that result in an increase in camber tend to exhibit higher lift coefficient. The flow is accelerated on the suction surface increasing the lift, drag and moment coefficients. Furthermore throughout the optimization process, maximum lift coefficients are obtained with almost maximum actuator authority. Meanwhile the design variable that corresponds to the extension of the active part of the camber reaches the lower limit of the constraint, which makes the effect of the actuator authority more profound, as it is observed from Figure 5. On the other hand the minimisation of the more sensitive pitching moment coefficient requires more subtle geometric changes dictating mediocre authority and active camber width as can be seen from Figure 6.

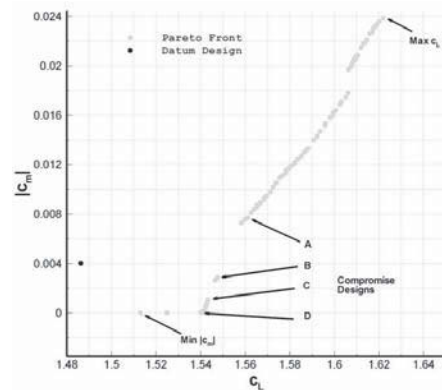


Figure 4. Optimization Pareto Front.

Table 2 summarizes the flow metrics of the optimization investigation. Overall, it is observed that the attainment of higher lift is in conflict with the need for low drag coefficients and pitching moment characteristics. Nevertheless, the methodologies applied in the MOBID system results in the identification of the design vectors that reveals aerodynamic performance gains over the reference airfoil design. The Pareto front provides a clear picture of the achievable trade-offs between the competing objectives.

Design	c_l	c_m	c_d
Datum	1.48625	0.00403	0.03543
Max. c_l	1.62183	-0.02388	0.04079
Min. c_m	1.51211	-0.00002	0.03671
Comp. A	1.55664	-0.00763	0.03889
Comp. B	1.54586	-0.00244	0.03888
Comp. C	1.54126	-0.00063	0.03874
Comp. D	1.53842	0.00039	0.03857

Table 2. Aerodynamic loads comparison amongst optimal designs.

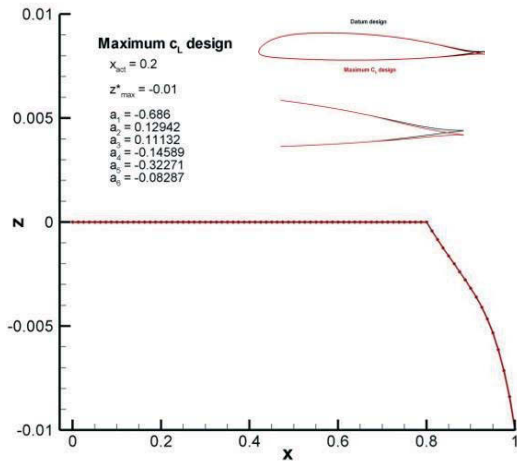


Figure 5. Maximum C_l design.

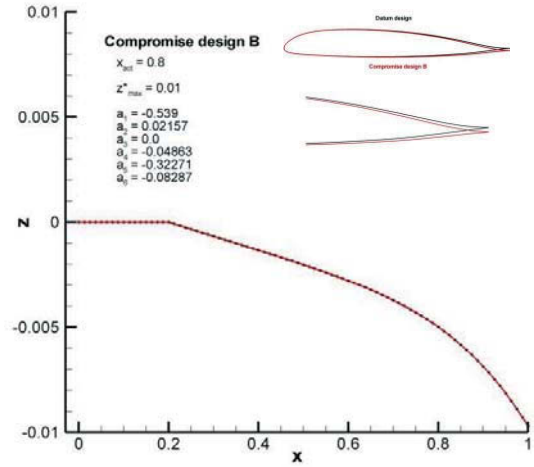


Figure 8. Compromise design B.

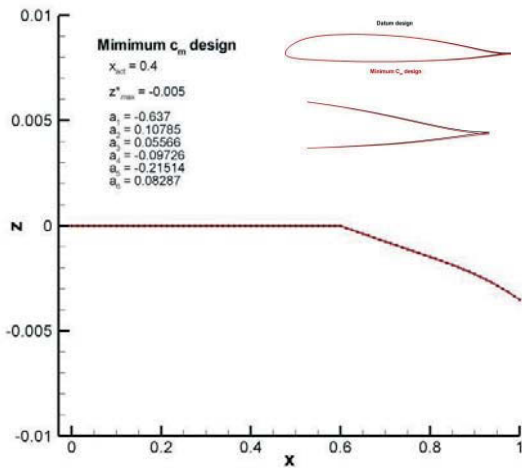


Figure 6. Maximum C_m design.

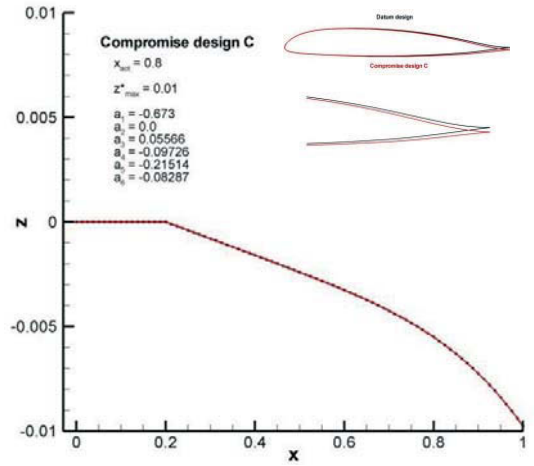


Figure 9. Compromise design C.

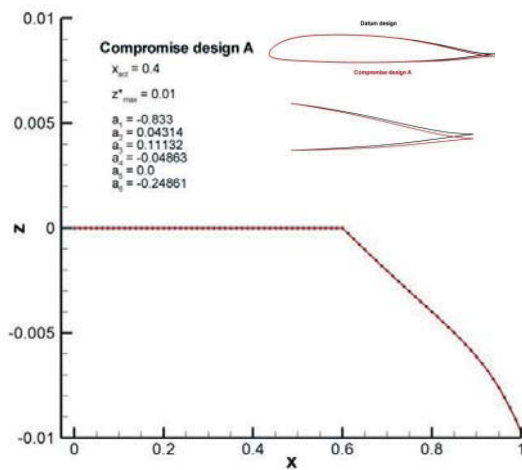


Figure 7. Compromise design A.

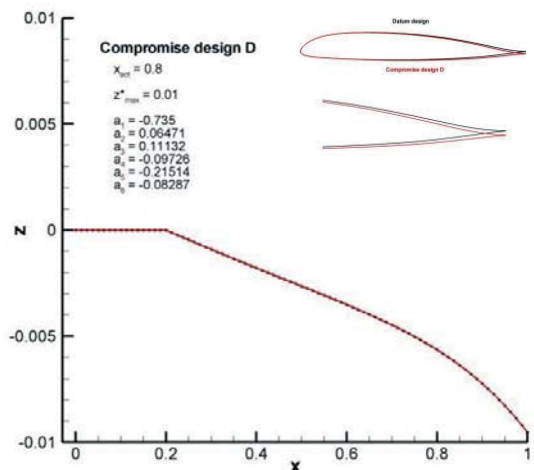


Figure 10. Compromise design D.

4. SMA BASED DEVICE DESIGN.

The proposed device concept is clearly depicted in Figure 11: a SMA rod is integrated within the blade structure and transmits, when heated, a torque couple which induces twist onto the blade.

The SMA rod in charge of producing the blade torsion is previously twisted thus achieving martensitic phase and then integrated within the blade. The elastic recovery of SMA material tends to twist the blade, whose reaction is exploited, after activation, for recovering initial (non twisted) blade condition.

In order to prepare and validate the test campaign carried out by CIRA and described in section 6, AERnnova has performed thermo-mechanical FEM simulations for several different boundary and load conditions by using commercially available MSC Marc/Mentat software. The main characteristics of the specimen used for tests and for simulations are: rod diameter: 5.5mm, operative rod length: 136mm, total rod length: 150mm, equal to operative tube length plus clamped and rotation application zone, both of 7mm. SMA typology is NiTiNOL 44.5-55.5 with the following material properties: austenite and martensite Young modulus $E_A=28160\text{MPa}$, $E_M=8780\text{MPa}$, thermal expansion coefficients $\alpha_A=11\cdot 10^{-6}\text{ }1/^\circ\text{C}$, $\alpha_M=6.6\cdot 10^{-6}\text{ }1/^\circ\text{C}$, $\nu_A=\nu_M=0.33$, yield stress of the pure austenite phase: 896MPa , yield stress of the pure martensitic phase: 834.6MPa , martensite and austenite start and finish temperature in stress-free condition $M_s^0=10^\circ\text{C}$, $M_f^0=-20^\circ\text{C}$, $A_s^0=39^\circ\text{C}$, $A_f^0=82^\circ\text{C}$, slopes of martensite and austenite start-finish temperatures $C_m=6.0\text{ MPa}/^\circ\text{C}$, $C_a=8.0\text{ MPa}/^\circ\text{C}$.

In the first step, two kind of analysis are performed for the SMA rod, thermal validation with an aim to demonstrate how SMA rod changes its internal structure with temperature (Shape Memory Effect, SME); and maximum recoverable angle validation, aiming at the validation of the results obtained by CIRA in its tests. Once validated with experimental results, the next step is integration of the SMA rod thermal actuator into different positions along the rotor blade FEM model (Figure 11-12) and corresponding tip twist angles are compared in order to obtain the best actuator position. If the priority is to achieve the highest twist angle at the blade tip, the optimum spanwise position of the SMA actuator is 0.9R (Figure 13). In all analyzed cases for this particular blade, the spanwise induced rotations present an identical behavior, a gradual increment from the blade root to the actuator position followed by a practically constant value until blade tip. Consequently, depending on desirable spanwise

twist variation and the twist tip value, the SMA actuator could be placed at different positions. For any SMA actuator position it is detected a zone in its nearness with a higher twist values due to high stress concentrations which appears due to actuator insertion in the spar.

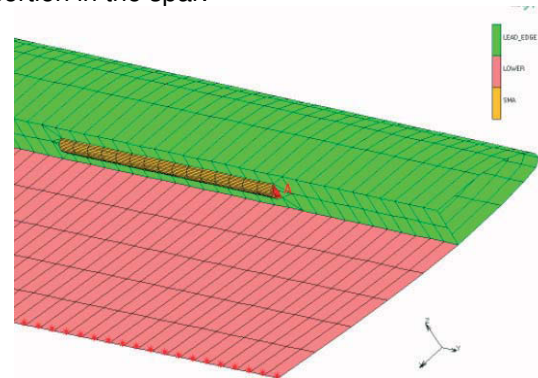


Figure 11. SMA actuator introduced at 0.9R position in a rotor blade.

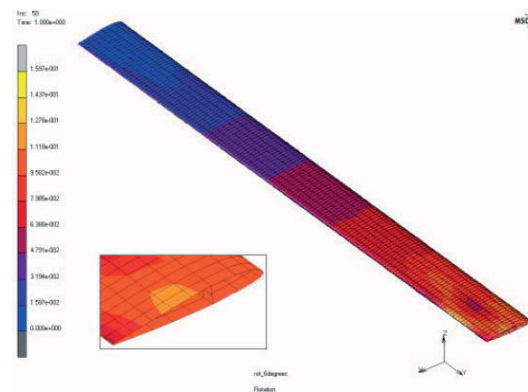


Figure 12. Rotated angle variation spanwise with SMA actuator at 0.9R.

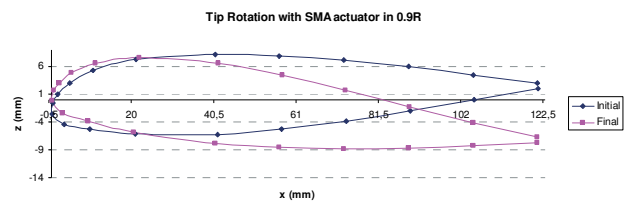


Figure 13. Tip blade rotation with SMA actuator at 0.9R.

5. MAIN ROTOR PERFORMANCE

Calculations are performed by using a simple numerical tool able to trim the rotors in axial flight.^[24] It is based on BEMT (Blade Element Momentum Theory) which is a methodology commonly used in preliminary design. The airfoil aerodynamics is taken into account either by assigning the properties such as the lift curve slope ($C_{l\alpha}$) or the profile drag (C_{d0}) or by extracting the aerodynamic coefficients from look-up tables. Several corrections have been implemented in order to take into account the effects

associated with Reynolds number, stall, tip losses, tip vortex.

In order to have a measure of the possible limitations of the tool, it is validated against the full scale rotor data published in [25]. Comparisons are included in Figure 14.

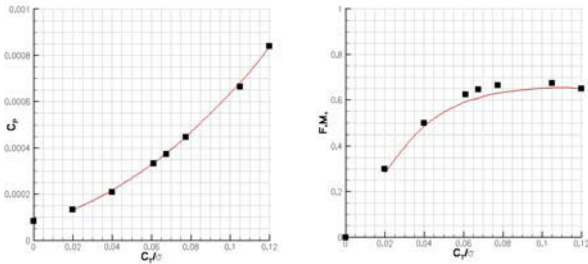


Figure 14: Rotor performances of the full scale rotor in terms of Power (left) and Figure of merit (right). Solid line = calculations; Symbols = experiments.

The performances of the model scale rotors are illustrated and compared in Figure 15. In particular, the effects of the parabolic tip and the influence of more aerodynamic efficient airfoils can be appreciated. The gain in terms of Figure of merit and power is remarkable.

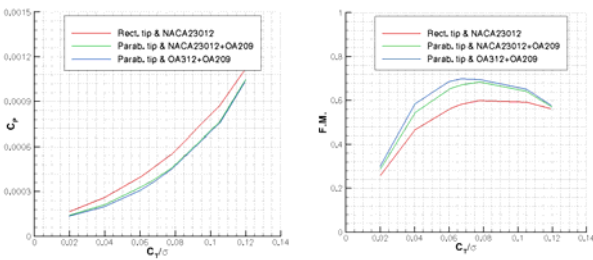


Figure 15: Performance predictions of the three model rotors considered in FRIENDCOPTER.

Before facing the problem of actuated twist, it is worth checking whether there is an optimum twist distribution starting from the built-in blade twist so that the aerodynamic performance is improved. It will be subsequently controlled if the new twist distribution could be provided by means of the actuation technology.

This exercise has been done as a single optimization problem where five design variables are used to modify the twist distribution. The objective function is built on the evaluation of the Figure of merit at several rotor loads with the constraint that the maximum sectional twist increment of 1 degree should not be exceeded. As far as the design variables, they are three twist values (at the blade root, at the tip and at an intermediate user defined blade radial station), the intermediate radial station and, finally, a parameter that can select one of the nine twist implemented distributions (linear, quadratic, ...).

The following rotor load conditions have been considered:

$$\frac{C_T}{\sigma} \Big|_{=0.02}, \quad \frac{C_T}{\sigma} \Big|_{=0.04}, \quad \frac{C_T}{\sigma} \Big|_{=0.066}, \quad \frac{C_T}{\sigma} \Big|_{=0.08}, \quad \frac{C_T}{\sigma} \Big|_{=0.10}, \quad \frac{C_T}{\sigma} \Big|_{=0.12}.$$

The objective function is:

$$FM \Big|_w = 0.10 FM \Big|_1 + 0.15 FM \Big|_2 + 0.25 FM \Big|_3 + 0.25 FM \Big|_4 + 0.15 FM \Big|_5 + 0.10 FM \Big|_6.$$

OPTIMUS,^[26] the integration and optimization software environment from Noesis solutions, is used. This software package is able to integrate arbitrary numerical analysis codes, to automate the process execution, to control data exchanges, to split the process over a heterogeneous computational environment where analysis codes run on different computer platforms, to post-process results. The key functionalities of optimization methods are available for addressing the search of global optima. DOE, RSM, Gradient/Genetic based algorithms can be, respectively, used for the exploration of the design space, the approximation of models, the design optimization.

The optimization process can best be described by looking at the OPTIMUS workflow graphical representation (Figure 16). It allows to see directly the steps necessary to evaluate the objectives (in red) starting from the design variables (in light blue) throughout the data exchange (in green) and the analysis blocks (in orange). Six parallel streams, one for each considered rotor load conditions, are set up to account for the effect of change in twist distribution on the rotor performance.

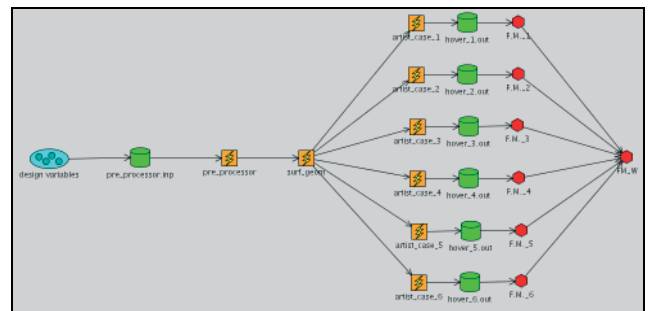


Figure 16. OPTIMUS workflow.

The pre-processor updates the input file of the surface grid generator according to the design variables set by the optimizer; after the surface grid is generated, the BEMT code computes the Figure of merit for each rotor load conditions which are subsequently used to evaluate the objective function. Several optimization problems have been performed. All of them have been based on a three-level full factorial Design of Experiment (DOE) followed by a

Response Surface Method (RSM) from which a differential evolution algorithm has been employed.

The first problem concerns the search of an optimum twist distribution assuming that the built-in twist can be modified all over the blade or on a limited portion of it. The first assumption corresponds to an actuator acting all along the blade whereas the latter assumption implies an integration of the actuator into a given blade segment. Three cases corresponding to different blade segments where the twist variation is made possible are considered: $r/R=[0.7, 1.0]$, $r/R=[0.45, 0.75]$, $r/R=[0.275, 0.525]$.

The optimum twist distributions found are represented in Figure 17. It can be seen that nearly the maximum bound of the design space has been chosen by the optimizer (that is, 1 degree) for each case. This fact suggests that actuators allowing larger twist variations are preferable.

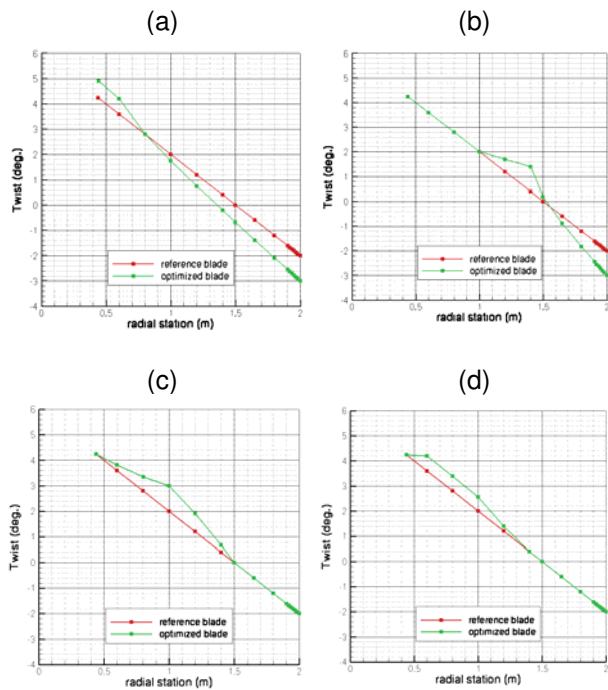


Figure 17: optimized twist distribution in the case of a twist variation in the range (a) $r/R=[0.275, 1.0]$, (b) $r/R=[0.7, 1.0]$, (c), $r/R=[0.45, 0.75]$, (d) $r/R=[0.275, 0.525]$.

The results in terms of the objective function are collected in Table 3 from which it can be concluded that it is convenient to act on the whole blade and, as alternative, to integrate the actuator in the outer part of the blade.

After these preliminary investigations, the AERnova-CIRA concept presented in section 4 is analyzed. In this case, the actuation technology is known, that is, depending on the location where the actuator is integrated, the maximum twist variations are known. Thus, the problem consists in searching

for the best place where the actuator has to be integrated and for the amount of the twist variation (provided by the actuator among the allowable ones) so that the hover performance is improved.

ID	Span wise range where twist variations are possible	Maximum allowed twist variation	FM_W
Twist _{ref}	-	-	0.60947
Twist _{all}	$r/R=[0.22, 1.0]$	± 1 deg.	0.62691
Twist _{out}	$r/R=[0.7, 1.0]$	± 1 deg.	0.61791
Twist _{med}	$r/R=[0.45, 0.75]$	± 1 deg.	0.61342
Twist _{inn}	$r/R=[0.275, 0.525]$	± 1 deg.	0.61346

Table 3. Summary of results.

The actuator consists of a SMA element 135 mm long, corresponding to 6.8% of the entire blade span. AERnova performed some numerical calculations to predict the maximum twist variation for a given number of actuator installation positions on the reference model rotor.

Since the actual twist laws all along the blade with the actuation 'on' is not available, specific twist laws are considered: in Figure 18, Figure 20 and Figure 22 the assumed twist distributions for SMA actuator located in the ranges $[0.9 - 0.968]$, $[0.7 - 0.768]$ and $[0.5 - 0.568]$ r/R , for both linear (mode 1) and parabolic (modes 2 and 3), positive (green) and negative (blue) torsion are illustrated.

A DOE (based on a latin-hypercube algorithm with 200 designs) is calculated using the same objective function previously defined for each actuator position. The results are sketched in Figure 19, Figure 21 and Figure 23, respectively.

By looking at the individual DOE results, the following conclusions can be drawn:

- negative twist variations result in performance improvements;
- the twist law affects significantly the performance calculations;
- the twist law labelled as mode-2 offers the most significant performance gain;
- the maximum twist variation is necessary to get the maximum performance gain.

Finally, a summary of the most promising results is reported in Table 4 and the associated figures of merit are compared in Figure 24. It clearly appears that the actuator integrated in range $r/R=[0.9 - 0.968]$, assures a better hover performance.

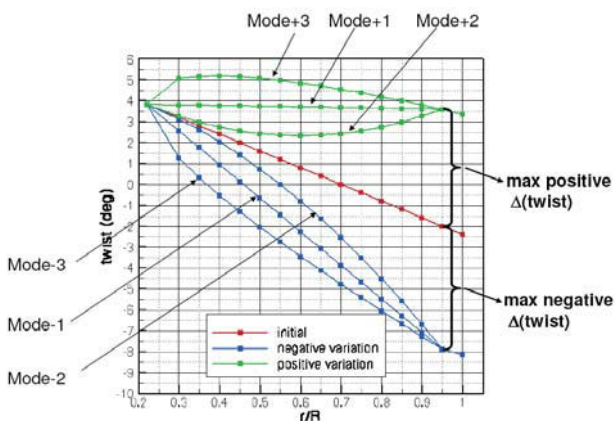


Figure 18. Twist distributions for SMA actuator located between 0.9 and 0.968 r/R: positive (green) and negative (blue), linear (mode 1) and parabolic (modes 2 and 3).

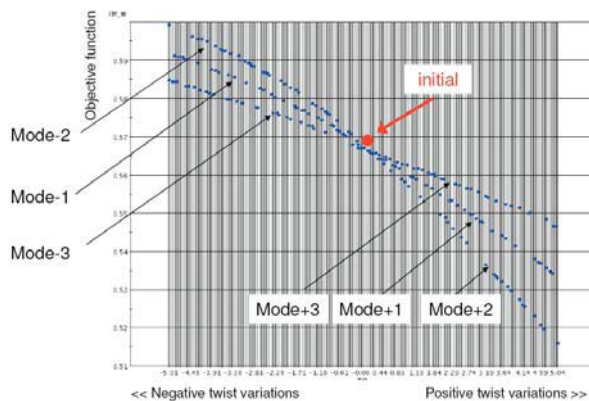


Figure 21. Objective function for SMA actuator located between 0.7 and 0.768 r/R.

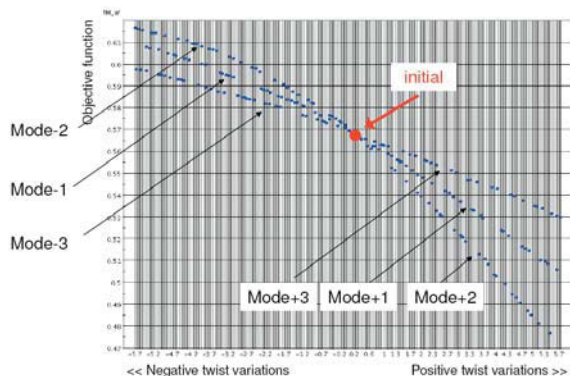


Figure 19. Objective function for SMA actuator located between 0.9 and 0.968 r/R.

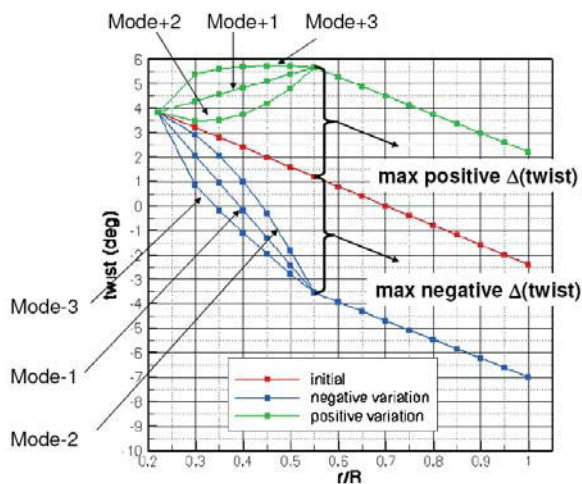


Figure 22. Twist distributions for SMA actuator located between 0.5 and 0.568 r/R: positive (green) and negative (blue), linear (mode 1) and parabolic (modes 2 and 3).

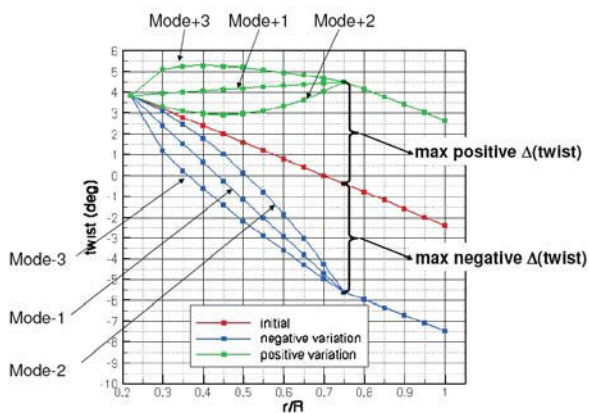


Figure 20. Twist distributions for SMA actuator located between 0.7 and 0.768 r/R: positive (green) and negative (blue), linear (mode 1) and parabolic (modes 2 and 3).

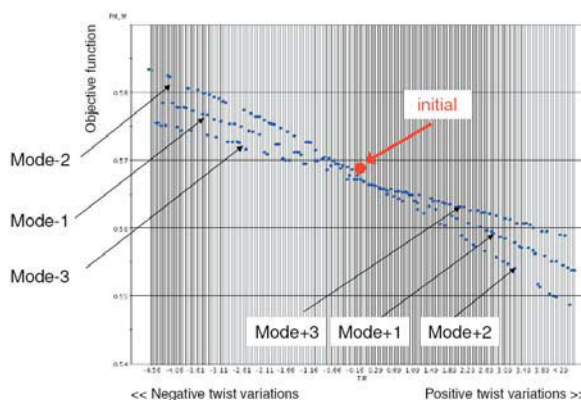


Figure 23. Objective function for SMA actuator located between 0.5 and 0.568 r/R.

IS	Spinning speed (RPM)	Maximum angular deformation (degrees)	Output torque (N.m)
Twist _{ref}	-	-	0.423
Twist _{ref} + 0.1	500 [0.22, 0.22]	-4.00°	0.572
Twist _{ref} + 0.2	500 [0.44, 0.44]	-8.00°	0.521
Twist _{ref} + 0.3	500 [0.66, 0.66]	-12.00°	0.519
Twist _{ref} + 0.4	500 [0.88, 0.88]	-16.00°	0.522
Twist _{ref} + 0.5	500 [1.10, 1.10]	-20.00°	0.523

Table 4. Summary of the results.

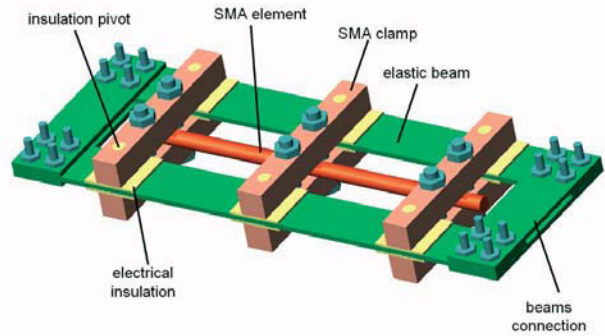


Figure 25. Torque demonstrator sketch.

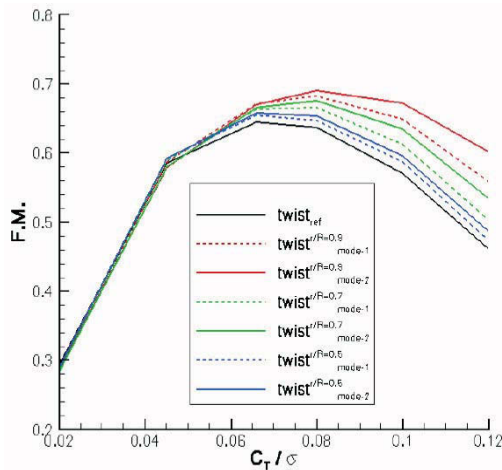


Figure 24. Figure of merit comparison for the several SMA twist distributions.

6. PROTOTYPE REALISATION AND TESTING

A prototype of the SMA device is designed and manufactured. As shown in the scheme of Figure 25, it is constituted by:

- a SMA rod element; this component is connected to surrounding structure by means of three clamps equally spaced along the length;
- SMA clamps, in charge of transmitting rotation to the structure;
- a surrounding structure made of elastic beams; in charge of providing restoring torque couple when the SMA is un-activated;
- layer electrical insulation; interposed between clamps and beams element, to assure electrical insulation;
- insulation pivots to prevent from any radial translation and to assure electrical insulation.

According with the scheme of Figure 25 a real prototype is manufactured. During the manufacturing process, a preliminary training phase (load and unload cycles) is necessary to keep constant SMA properties during operative life, up to reach a satisfying repeatability level.

Then, the SMA edges is connected to a home made machine aimed at producing torque and a suitable angular pre-deformation has been impressed, to assure entire transformation of austenite into martensitic phase.

After mounting the elastic plates around the SMA rod, one edge is released, allowing for a partial rotation recovery, resulting in a compromise between structure and SMA elastic reactions. Residual stress assures SMA to return into initial no-activated configuration, after cooling.

Once manufacturing and preliminary training operations are addressed, a dedicated experimental setup is assembled, integrating SMA device and mechanism in charge of twisting with: an angular sensor (electro-transducer) to measure all the rotations; a thermocouple bonded on the SMA rod to measure the actual temperature; an acquisition system to collect data provided by the angular sensor and the thermocouple; a power supplier to heat by Joule effect the SMA rod; a signal generator to generate a logical signal (a square wave) to command the switch on (heating phase) and switch off (cooling phase) of the SMA element, for cyclic tests; a thermocouple digital displayer, to have a digital estimate of the actual temperature.

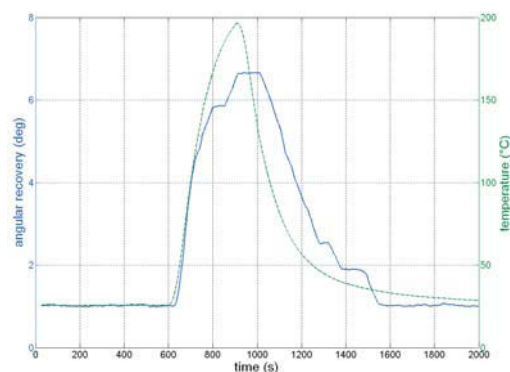


Figure 26. Temperature and angular rotations within a cycle are plotted vs. time.

Different activation cycles are carried out: a current of 70.0 A is used to reach a SMA temperature of 200 °C (above which no further rotations are observed), and then the SMA element is let cool by natural convection, up to reach the initial room temperature (27.0 °C).

A max angular rotation of 6 deg, for a temperature of 198 °C has been measured (Figure 26). Through a FE comparative model of the prototype, the transmitted moment corresponding to such an induced rotation has been computed: 21.6 Nm.

7. CONCLUSIONS AND FURTHER STEPS

In the present work the idea of modifying actively the blade twist through a SMA based device, suitably integrated along spanwise direction, has been illustrated. The research activity has dealt with numerical studies and experimental testing of a prototype. The capabilities of the device to induce twist variations have been demonstrated and the potential benefits have been estimated for hover conditions in terms of Figure of merit.

Further investigations, both theoretical and experimental, will be carried out in the near future; a more detailed design of the device is envisaged to accurately define some critical components (e.g. the clamps in charge of transmitting rotations); moreover, a dedicated manufacturing process, oriented to SMA integration within a real blade, is at the moment under definition; finally, dedicated tests aimed at appreciating device performance during a cyclic life are envisaged, to achieve a final product of interest for the aerospace industry.

8. ACKNOWLEDGEMENTS

The present work has been carried out within the FRIENDCOPTER integrated project co-funded by the European Commission.

9. REFERENCES

- [1] Integrated Project of the European 6th Framework Programme: "Integration of Technologies in Support of a Passenger and Environmentally Friendly Helicopter", www.friendcopter.org.
- [2] Enenkl, B.: "1/2.5 Scaled Model Rotor of the Hingeless BO105 Main Rotor.", MBB Technical Documentation, 26.10.1988.
- [3] Chopra, I., "Review of State of Art of Smart Structures and Integrated Systems", 42nd AIAA/ ASME/ASCE/AHS/ASC Structures, Structural Dynamics, and Materials Conference, Seattle, WA, AIAA Journal 40(11), (2002).
- [4] Chopra, I., Status of Application of Smart Structures Technology to Rotorcraft Systems, presented at the Innovation in Rotorcraft Technology, Royal Aeronautical Society, London, UK, June 25-26, 1997 and AHS Journal, October 2002.
- [5] W.J. Buehler, J.V. Gilfrich, R.C. Wiley, 1963, "Effect of low-temperature phase changes on the mechanical properties of alloys near composition TiNi", Journal of Applied Physics 34, 1475 (1963).
- [6] L.C. Brinson, A. Bekker, M. Huang, "Deformation of Shape Memory Alloys due to Thermo-Induced Transformation", J. of Intelligent Material Systems and Structures 7(1), 97-107 (1996).
- [7] C. Liang and C.A. Rogers, "One-Dimensional Thermomechanical Constitutive Relations for Shape Memory Material", J. of Intelligent Material Systems and Structures 1(2), 207-234 (1990).
- [8] K. Tanaka, "A Thermomechanical Sketch of Shape Memory Effect: One-Dimensional Tensile Behaviour", Res. Mech. 18(3), 251-263 (1986).
- [9] Davidson, F.M., Liang, C., Lobitz, D.W., Investigation of Torsional Shape Memory Alloy Actuators, Proc. SPIE Vol. 2717, p. 672-682, Smart Structures and Materials 1996: Smart Structures and Integrated Systems, Inderjit Chopra; Ed.
- [10] Liang, C., Davidson, F. M., Schetky, L. M., Straub, F. K., Applications of torsional shape memory alloy actuators for active rotor blade control: opportunities and limitations, Proc. SPIE Vol. 2717, p. 91-100, Smart Structures and Materials 1996: Smart Structures and Integrated Systems, Inderjit Chopra; Ed.
- [11] Jayasimha, A. and Chopra, I., Behavior of Torsional Shape Memory Alloy Actuators, 44th AIAA/ASME/ASCE/AHS Conference, 7-10 April 2003, Norfolk, Virginia.
- [12] Prahlad, H. and Chopra, I., Characterization of SMA Torsional Actuators for Active Twist of Tilt Rotor Blades, 43rd AIAA/ASME/ASCE/AHS/ASC Conference, 22-25 April 2002, Denver, Colorado.
- [13] Prahlad, H. and Chopra, I., Modeling and experimental characterization of SMA torsional actuators, Journal of intelligent material systems and structures, 2007, vol. 18, no1, pp. 29-38.
- [14] Altmikus, A.A. and Bailly, B.J., "FRIENDCOPTER Report on Reference Rotor," Deliverable No. : D 5.1-2 ,17 May 2005.
- [15] Schultz, K.J., Spletstoeser, W., Junker, B., Wagner, W., Schoell, E., Arnauld, G. Mercker, E., Pengel, K., Fertis, D., "A Parametric Wind Tunnel Test on Rotorcraft Aerodynamics and Aeroacoustics (HELISHAPE) – Test Documentation and Representative Results -," DLR IB 129-96/25, June 1996.
- [16] www.pointwise.com/gridgen.
- [17] Toro, E. F., Spruce, M., and Speares, W., "Restoration of the contact surface in the HLL-Riemann solver," Shock Waves, Vol. 4, No. 1, 1994, pp. 25–34.
- [18] D. Drikakis, F. Durst "Investigation of flux formulae in shock wave turbulent boundary layer interaction," International Journal for Numerical Methods in Fluids, Vol. 18, pp. 385-413, 1994.
- [19] D. Drikakis, "Advances in turbulent flow computations using high-resolution methods," Progress in Aerospace Science, 39, 405-424, 2003.
- [20] Shu, C.W., Essentially Non-Oscillatory and Weighted Essentially Non-Oscillatory Schemes for Hyperbolic Conservation Laws. NASA CR-97-206253, (1997).
- [21] Steger, J. L. and Warming, R. F., "Flux vector splitting of the inviscid gasdynamic equations with application to finite-difference methods," Journal of Computational Physics, Vol. 40, 1981, pp. 263–293.
- [22] D. Drikakis, S. Tsangaris "On the solution of the compressible Navier-Stokes equations using improved flux vector splitting methods," Applied Mathematical Modelling, Vol. 17, pp. 282-297, 1993.
- [23] Jaeggi, D. M., Asselin-Miller, C. S., Parks, G. T., Kipouros, T., Bell, T., and Clarkson, P. J. Multi-Objective Parallel Tabu Search. Lecture Notes in Computer Science, 3242:732–741, (2004).
- [24] Pagano, A., "Investigations within the ADYN Project: a Year of Activities," CIRA doc. N. CIRA-TR-02-503, January 2003.
- [25] Warmbrodt, W. and Peterson, R.L., "Hover Test of a Full-Scale Hingeless Rotor," NASA Technical Memorandum 85990, August 1984.
- [26] OPTIMUS, Optimization environment, Software Package, Ver. 5.2, Noesis solutions, Belgium, 2006.